

Room-temperature chiral magnetic skyrmions in ultrathin magnetic nanostructures

Olivier Boulle^{1,2,3*}, Jan Vogel^{4,5}, Hongxin Yang^{1,2,3}, Stefania Pizzini^{4,5}, Dayane de Souza Chaves^{4,5}, Andrea Locatelli⁶, Tevfik Onur Menteş⁶, Alessandro Sala⁶, Liliana D. Buda-Prejbeanu^{1,2,3}, Olivier Klein^{1,2,3}, Mohamed Belmeguenai⁷, Yves Roussigné⁷, Andrey Stashkevich⁷, Salim Mourad Chérif⁷, Lucia Aballe⁸, Michael Foerster⁸, Mairbek Chshiev^{1,2,3}, Stéphane Auffret^{1,2,3}, Ioan Mihai Miron^{1,2,3} and Gilles Gaudin^{1,2,3}

Magnetic skyrmions are chiral spin structures with a whirling configuration. Their topological properties, nanometre size and the fact that they can be moved by small current densities have opened a new paradigm for the manipulation of magnetization at the nanoscale. Chiral skyrmion structures have so far been experimentally demonstrated only in bulk materials and in epitaxial ultrathin films, and under an external magnetic field or at low temperature. Here, we report on the observation of stable skyrmions in sputtered ultrathin Pt/Co/MgO nanostructures at room temperature and zero external magnetic field. We use high lateral resolution X-ray magnetic circular dichroism microscopy to image their chiral Néel internal structure, which we explain as due to the large strength of the Dzyaloshinskii–Moriya interaction as revealed by spin wave spectroscopy measurements. Our results are substantiated by micromagnetic simulations and numerical models, which allow the identification of the physical mechanisms governing the size and stability of the skyrmions.

The recent discovery of nanometre-size whirling magnetic structures named magnetic skyrmions has opened a new path to manipulate magnetization at the nanoscale^{1–7}. A key feature of such magnetic nano-objects is their chiral and topologically non-trivial spin structure, that is, their magnetization texture cannot be continuously transformed into the uniform magnetic state without causing a singularity⁸. For a surface C , this topological property is characterized by the skyrmion number $S = (1/4\pi) \int_C \mathbf{m} \cdot ((\partial \mathbf{m} / \partial x) \times (\partial \mathbf{m} / \partial y)) dx dy$, where \mathbf{m} is the normalized magnetization vector. For a single skyrmion, $|S|$ is quantized and equal to 1 whereas $S = 0$ for the ferromagnetic state or any topologically trivial structure. The skyrmion chiral property is generally driven^{2,6} by an additional antisymmetric term in the exchange energy, namely the Dzyaloshinskii–Moriya interaction (DMI), induced by the spin–orbit coupling and the lack of structural inversion symmetry^{9,10}. This additional energy term $E_{\text{DM}} = \mathbf{D} \cdot (\mathbf{S}_1 \times \mathbf{S}_2)$ where \mathbf{D} is the DMI characteristic vector and \mathbf{S}_1 and \mathbf{S}_2 are two neighbouring spins. Thus, the DMI tends to make the magnetization rotate around \mathbf{D} . Another important feature is that skyrmions can be manipulated by in-plane currents^{11–14}, which has led to novel concepts of non-volatile magnetic memories^{7,15} and logic devices¹⁶ where skyrmions in nanotracks are the information carriers. The nanometre size of the skyrmions combined with the low current density needed to induce their motion^{11,13,14} would lead to devices with an unprecedented combination of high storage density, high data transfer rate and low power consumption^{7,15}. The topological ($|S| = 1$) and chiral properties of skyrmions are keys for such devices as they control the current-induced skyrmion dynamics^{7,14,17–20} and

the interaction of skyrmions with other spin structures and the nanostructure edges^{16,19–23}.

Although predicted at the end of the 1980s¹, chiral skyrmion lattices and isolated skyrmions were observed only recently in B20-type bulk or thin film chiral magnets⁶ such as MnSi (ref. 3), Fe_{1–x}Co_xSi (ref. 24), FeGe (ref. 25), Mn_{1–x}Fe_xGe (ref. 26) and in ultrathin magnetic films composed of Fe or PdFe monolayers on Ir(111)^{27–29}. In B20 magnets, the DMI results from the non-centrosymmetric crystalline structure and Bloch-like skyrmions have been observed below room temperature²⁵ and in the presence of an external magnetic field⁶. In epitaxial heavy metal/ferromagnetic ultrathin films^{27–29}, the DMI arises from the breaking of inversion symmetry at the interfaces combined with the large spin–orbit coupling in the heavy metal⁷, leading to skyrmions with a Néel-like structure^{30,31}. However, the observed skyrmions were stable only at low temperature³², which prevents any use for room-temperature applications. In addition, the ultrathin films were grown by molecular beam epitaxy, which is not suitable for industrial production.

Recently, the attention has shifted to ultrathin ferromagnetic/heavy metal films deposited by sputtering³³. This class of materials combines several features that make their use appealing for the study of skyrmion structures and their applications: (i) the magnetic parameters controlling the skyrmion stability and size, that is, the anisotropy, DMI and exchange^{30,34}, can be easily tuned by playing with the nature and thickness of the materials that comprise the multilayers; (ii) they are characterized by a large DMI^{35–42} that leads to chiral Néel domain walls (DWs)^{43,44}; (iii) large current-induced spin–orbit torques are present^{45,46}, which results in fast current-induced DW motion^{47,48}; and (iv) the deposition by

¹Univ. Grenoble Alpes, SPINTEC, Grenoble F-38000, France. ²CNRS, SPINTEC, Grenoble F-38000, France. ³CEA, INAC-SPINTEC, Grenoble F-38000, France. ⁴CNRS, Institut Néel, 25 avenue des Martyrs, B.P. 166, Grenoble Cedex 9 38042, France. ⁵Univ. Grenoble Alpes, Institut Néel, 25 avenue des Martyrs, B.P. 166, Grenoble Cedex 9 38042, France. ⁶Elettra-Sincrotrone, S.C.p.A., S.S. 14 - km 163.5 in AREA Science Park 34149 Basovizza, Trieste, Italy. ⁷LSPM (CNRS-UPR 3407), Université Paris 13, Sorbonne Paris Cité, 99 avenue Jean-Baptiste Clément, Villetaneuse 93430, France. ⁸ALBA Synchrotron Light Facility, Carretera BP 1413, Km. 3.3, Cerdanyola del Vallès, Barcelona 08290, Spain. *e-mail: olivier.boulle@cea.fr

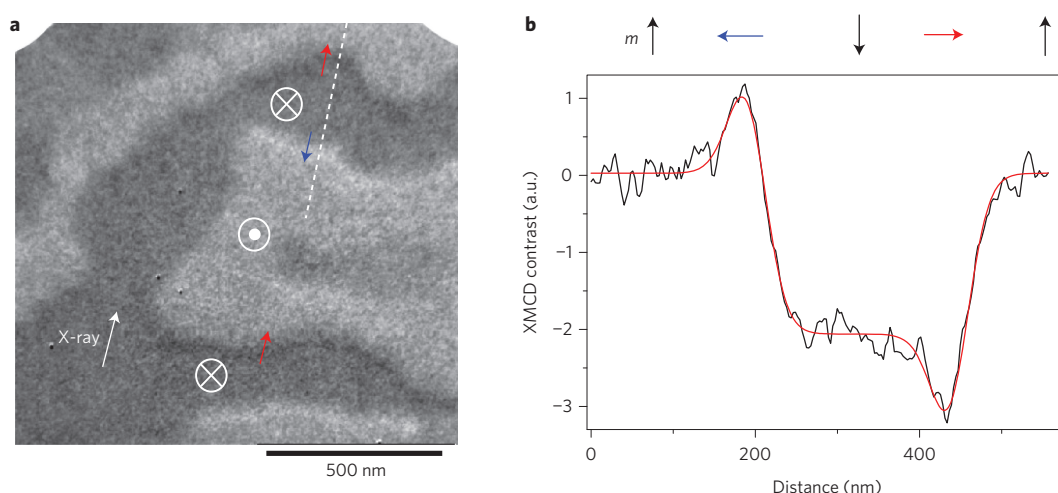


Figure 1 | Imaging of the chiral Néel structure of domain walls using XMCD-PEEM magnetic microscopy. **a**, Magnetic image of a multidomain state in a continuous Pt/Co/MgO film. For DWs lying perpendicular to the X-ray beam direction, thin white and black lines can be seen, corresponding to the magnetization being aligned antiparallel and parallel to the photon beam, respectively. This demonstrates their chiral Néel structure. **b**, Linescan of the magnetic contrast corresponding to the dotted white line in **a**. To reduce the noise, the contrast has been averaged perpendicularly to the linescan over 60 nm. The red line is a fit assuming a chiral Néel DW structure convoluted by a Gaussian function to take into account the finite spatial resolution (see Supplementary Information).

sputtering is fast and spatially homogeneous and is compatible with standard spintronic devices such as magnetic tunnel junctions, which makes the industrial integration straightforward. Whereas several recent experimental works have studied magnetic bubbles in these materials^{14,18,49,50}, and demonstrated their current induced motion^{14,50}, the direct evidence of their chiral internal structure is still lacking. Here we report on the observation of stable chiral skyrmions in sputtered ultrathin Pt/Co(1 nm)/MgO nanostructures at room temperature and zero applied magnetic field. We used photoemission electron microscopy combined with X-ray magnetic circular dichroism (XMCD-PEEM) to demonstrate their chiral Néel internal structure. The XMCD-PEEM combines several advantages for the observation of magnetic nanostructures, such as skyrmions: first, a high lateral spatial resolution (down to 25 nm); second, the magnetic contrast is proportional to the projection of the local magnetization along the X-ray beam direction. In our experiment, the X-ray beam impinges at a grazing angle of 16° on the sample surface plane so that the contrast is approximately three times larger for the in-plane component of the magnetization than for the out-of-plane one. This important feature allows the direct imaging of the internal in-plane spin structure of DWs or skyrmions.

Observation of chiral Néel domain walls

All images shown here were acquired at room temperature and, unless otherwise stated, no external magnetic field was applied during the experiments. The PEEM observations were done in a virgin demagnetized state obtained after nanofabrication and annealing of the sample. Complementary magnetization measurements on unpatterned thin films show that the magnetization in the domains is oriented perpendicularly to the film plane, which is due to a large interfacial uniaxial anisotropy. Figure 1a shows an XMCD-PEEM magnetic image of a multidomain state in the continuous film. Bright and dark grey regions correspond respectively to the magnetization pointing up and down. Interestingly, we observe a sharp increase in the dichroic contrast for DWs perpendicular to the X-ray beam, with a strong dark contrast when going from a down- to an up-magnetized domain (along the beam direction) and a strong bright contrast when going from an up- to a down-magnetized domain. This can be seen more easily in the linescan of the magnetic contrast shown in Fig. 1b, corresponding to the white dashed line in

Fig. 1a. A peak in the contrast is observed at the up/down DW position while a dip is observed at the down/up DW position. Thus, the magnetization in the up/down DW is aligned antiparallel to the in-plane direction of the X-ray beam whereas the magnetization in the down/up DW is aligned parallel. We conclude that the DW magnetization is perpendicular to the DW surface with an opposite magnetization direction for the two DWs. This demonstrates that DWs in this material are chiral Néel DWs with a left-handed chirality. Note that for Bloch DWs, the magnetization would be always perpendicular to the beam direction so that no peak or dip in the magnetic contrast should be observed. The linescan is well-fitted assuming a chiral Néel DW structure, the finite resolution of the instrument being modelled by a Gaussian convolution (red curve, Fig. 1b). The fit leads to a DW width of 29.5 ± 4 nm ($\pi\sqrt{A/K_{\text{eff}}}$) (see Supplementary Information).

Large DM interaction in Pt/Co/MgO thin films

The driving force of the DW and skyrmion chiral structure is the DMI. To further quantify its strength in our films, we carried out spin wave spectroscopy experiments using a Brillouin light scattering (BLS) technique in the Damon-Eshbach geometry (see Supplementary Information)⁴¹. This allows us to extract a DM parameter $D = 2.05 \pm 0.3$ mJ m⁻². As D is expected to be inversely proportional to the film thickness t (refs 39,41,42), one can define a related interfacial DM parameter D_s such that $D = D_s/t$ and we find a value $D_s = 2.17 \pm 0.14$ pJ m⁻¹. To our knowledge, this value is the highest reported so far for a sputtered magnetic ultrathin film. To better understand this large value, we carried out *ab initio* calculations of the DMI in Pt/Co/vacuum and Pt/Co/MgO multilayers (see Supplementary Information)⁴². For 5 monolayers (ML) of Co, equivalent to a total Co thickness of 1 nm, the *ab initio* calculations predict $D = 2.3$ mJ m⁻² in relatively good agreement with experiments, whereas a lower value $D = 1.5$ mJ m⁻² is predicted for a Pt/Co/vacuum structure. To explain this enhancement, we calculated a layer resolved map of the DMI by imposing a spin spiral on one monolayer whereas the other layers stay in a ferromagnetic alignment⁴². We show in Fig. 2 the resulting map for Pt/Co(3 ML)/vacuum and Pt/Co(3 ML)/MgO multilayers. The calculations show that for both multilayers, the DMI is largest at the first Co ML and thus mainly arises from the Pt/Co interface.

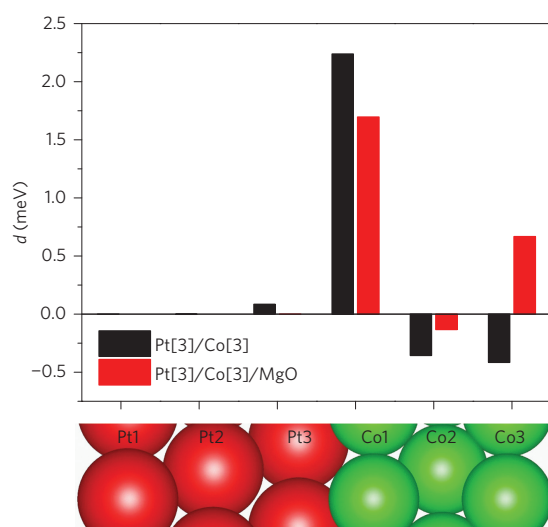


Figure 2 | Layer-resolved amplitude of the microscopic DMI for Pt[3 ML]/Co[3 ML] and Pt[3 ML]/Co[3 ML]/MgO obtained with *ab initio* calculations.

A significant contribution is also observed at the last Co ML at the vacuum (resp. MgO) interface. However, while it is negative for the Co/vacuum interface, and thus decreases the total D value, it is positive at the Co/MgO interface. The large DMI amplitude in Pt/Co/MgO can thus be explained by a significant additional contribution at the Co/MgO interface, which has the same sign as the one at the Pt/Co interface and thus enhances the total DMI.

Room-temperature magnetic skyrmions

In continuous thin films, isolated magnetic bubbles⁵¹ or chiral skyrmions⁶ have been observed so far in the presence of a perpendicular magnetic field, which breaks the stripe domains or helical structure driven by the magnetostatic or DM energy. However, it is known that single magnetic bubbles can be stabilized without external magnetic fields using geometrical confinement in patterned nanostructures^{52,53}. Here we patterned different structures with various sizes and shapes (circular, square) in our Pt/Co/MgO thin films. Figure 3a shows a circular magnetic domain stabilized in the middle of a 420 nm wide square dot, imaged at room temperature and zero applied magnetic field. As observed in the

multidomain structure, a sharp black/white contrast is observed at the DW position at the bottom/top of the central domain. This leads to a dip/peak in the dichroic contrast when doing a linescan along the domain diameter in the beam direction (see Fig. 3b). This indicates that the in-plane DW magnetization is aligned parallel/antiparallel to the X-ray beam at the bottom/top of the reversed domain, that is, the DW surrounding the circular domain is a chiral Néel DW. This chiral border leads to a skyrmion number $|S| = 1$ for this structure. This demonstrates that the observed circular domain is a Néel-like magnetic skyrmion. To extract the size of the skyrmion from the image, we assume that the magnetization profile can be described by a 360° DW profile^{29,54,55}: $\mathbf{m} = \sin \theta(r)\mathbf{u}_r + \cos \theta(r)\mathbf{u}_z$ with $\theta(r) = \theta_{\text{DW}}(r - d/2) + \theta_{\text{DW}}(r + d/2)$, where $\theta_{\text{DW}}(r) = 2 \arctan[\exp(r/\Delta)]$; d is the skyrmion diameter, Δ the domain width, and \mathbf{u}_r the polar unit vector. The blue curve (Fig. 3b) shows a fit of the experimental linescan assuming a Gaussian convoluted 360° DW and a good agreement is obtained with experimental data. From the fit, a skyrmion diameter $d = 130 \pm 2.5$ nm is extracted.

To better understand these experimental results, we carried out micromagnetic simulations using experimental values for the magnetocrystalline anisotropy constant K , the magnetic moment per surface area and the DMI interaction amplitude \mathbf{D} . The exchange constant was used as a free parameter and the best agreement between experiments and micromagnetic simulations is obtained for $A = 27.5$ pJ m⁻¹, a value in line with previous measurements of A in ultrathin magnetic multilayers⁵⁶. Using these parameters, micromagnetic simulations predict a stable left-handed chiral skyrmion structure at zero external magnetic field (see Fig. 4a) with a diameter of 128 nm and a DW width of 37 nm. From this magnetization pattern, an experimental magnetic image can be simulated and a good agreement is obtained with the experimental results (see Fig. 4b and Fig. 3b, orange curve for the simulated linescan). Finally, the simulations allow us to reconstruct the structure of the observed skyrmion. In Fig. 4c we present a linescan of the in-plane (m_x) and out-of-plane (m_z) component of the magnetization along the skyrmion diameter, as predicted by the micromagnetic simulation. The skyrmion diameter (~ 130 nm) being large compared with the DW width (37 nm), the magnetization profile is close to two independent chiral Néel DWs, as can be seen on the m_z profile.

To study the effect of small perturbations on the skyrmion structure, we carried out further imaging experiments in the presence of a perpendicular external magnetic field H_z . In these experiments, a

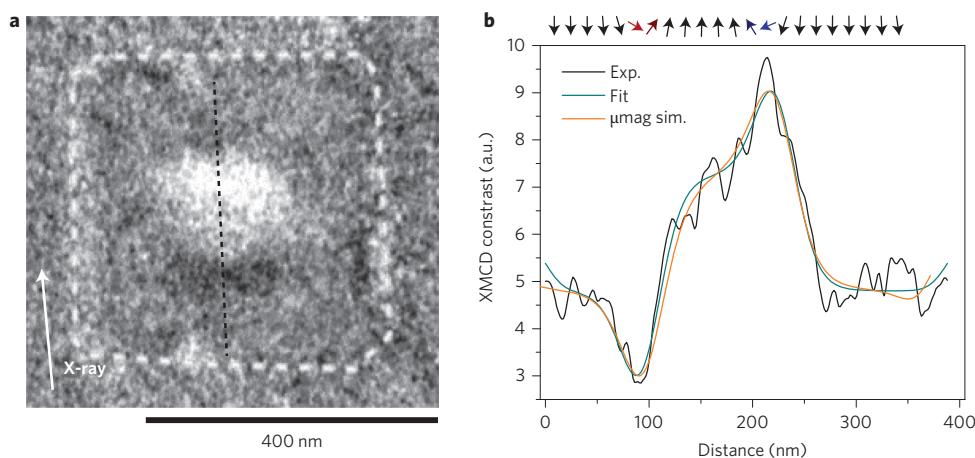


Figure 3 | Magnetic skyrmion observed at room temperature and zero external magnetic field. **a**, XMCD-PEEM image of a 420 nm square dot (indicated by the dotted line). **b**, Linescan along the dotted black line in **a**. The linescan has been averaged perpendicularly to the linescan over 30 nm. The blue line is a fit to the data using a Gaussian convoluted 360° DW profile (see Supplementary Information). The orange line is the contrast predicted by the micromagnetic simulations.

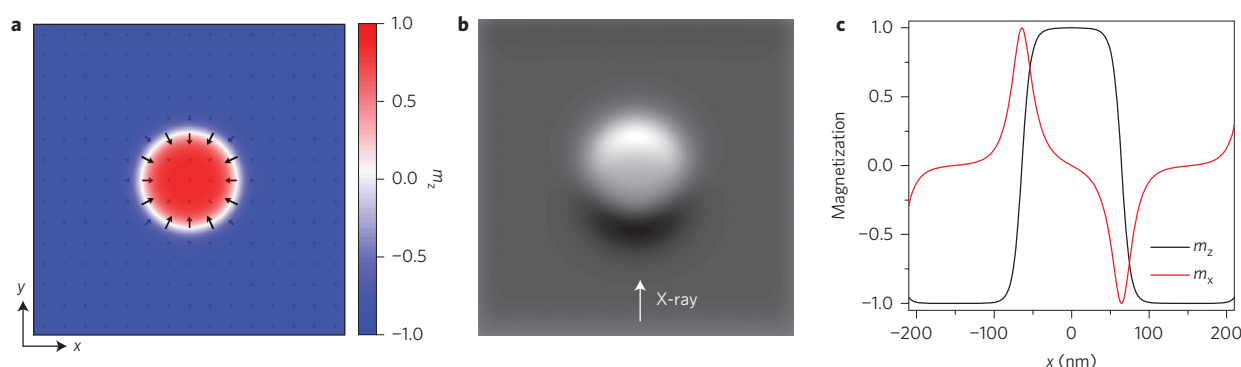


Figure 4 | Micromagnetic simulations. **a,b**, Distribution of magnetization (**a**) and simulated magnetic contrast (**b**) of the magnetic skyrmion in a 420 nm dot. **c**, Simulated magnetization component m_x and m_z along the skyrmion diameter ($y = 0$ axis).

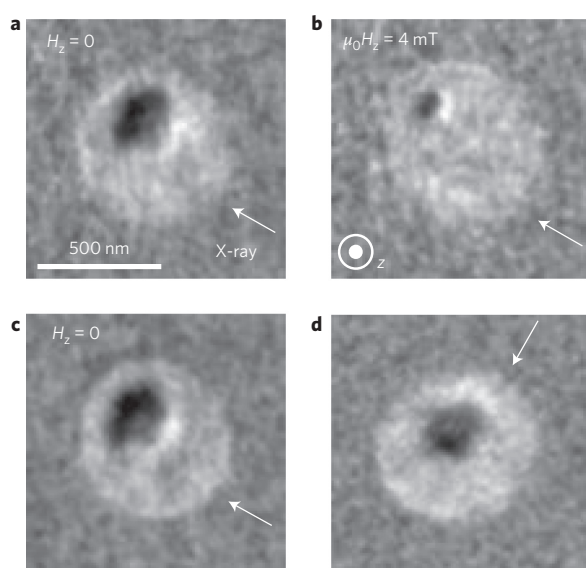


Figure 5 | Effect of an external perpendicular magnetic field. **a**, XMCD-PEEM image of a magnetic skyrmion in a 630-nm-diameter circular dot. **b**, XMCD-PEEM image of the same skyrmion during the application of an external magnetic field perpendicular to the film plane $\mu_0 H_z = 4$ mT. **c**, Image taken after **b** for $H_z = 0$. **d**, XMCD-PEEM image of the skyrmion after rotation of the sample by 90° with respect to the X-ray beam direction. The white arrows indicate the direction of the X-ray beam.

Pt/Co/MgO film with a slightly thicker Co layer (1.08 nm) was used. Figure 5a shows the XMCD-PEEM image of a magnetic skyrmion in a 630 nm diameter circular dot. The larger skyrmion diameter (190 nm) can be explained by the larger Co thickness, as predicted by the micromagnetic simulations (see Fig. 6b). Note that in this case, the skyrmion is not located in the centre of the dot, probably because of its pinning on a local defect. When applying a field $\mu_0 H_z = 4$ mT (Fig. 5b) in the direction opposite to the skyrmion core magnetization, the diameter of the skyrmion decreases down to 70 nm. When releasing the external magnetic field, the initial skyrmion structure is recovered (Fig. 5c). This demonstrates that the skyrmion structure is stable and reversible with respect to perturbations and that the skyrmion diameter can be tuned using H_z . To confirm the chiral structure of the skyrmion, we also imaged the skyrmion for an X-ray beam direction rotated by 90° in-plane with respect to the sample (Fig. 5d). As expected, the black/white contrast is now rotated by 90° which confirms the full radial orientation of the in-plane spins outward from the skyrmion centre and thus its chiral Néel structure.

Numerical calculations

The observation of stable skyrmions at zero external magnetic field raises the question of the physical mechanisms that govern the skyrmion stability and size in our experiments. To address this point, we consider a simple model where the magnetization in the dot $\theta(r)$ is described by a circular 360° Néel DW profile. The free energy E in the circular dot-shaped nanostructure can be written as the sum of two terms^{1,30,34,57}: (1) the skyrmion energy $E_\sigma[\theta(r)]$ due to the exchange, anisotropy and internal DW stray field energies; and (2) the energy due to the magnetostatic interactions between the domains E_{mag} . Assuming a radial symmetry, $E_\sigma[\theta(r)]$ can be written as^{1,30,34,57}:

$$E_\sigma[\theta(r)] = 2\pi t \int_0^R \left\{ A \left[\left(\frac{d\theta}{dr} \right)^2 + \frac{\sin^2 \theta}{r^2} \right] - D \left[\frac{d\theta}{dr} + \frac{\cos \theta \sin \theta}{r} \right] + (K_{\text{eff}} + E_{\text{DW}}^s) \sin^2 \theta \right\} r dr \quad (1)$$

where $K_{\text{eff}} = K - \mu_0 M_s^2 (1 - N_{\text{DW}})/2$ is the effective anisotropy^{54,58} (K is the magneto-crystalline anisotropy constant), t is the film thickness, R the dot radius. The demagnetizing energy due to the magnetic charges within the DWs E_{DW}^s is described by a constant demagnetizing factor N_{DW} such that $E_{\text{DW}}^s = N_{\text{DW}} \mu_0 M_s^2 / 2$. The energies E_σ and E_{mag} ⁵⁹ can be calculated as a function of the skyrmion diameter d assuming a 360° DW profile and a 420-nm-diameter circular dot (the magnetic parameters correspond to the experiment of Fig. 3, see methods). More physical insight is obtained from the effective forces $F_\sigma(d) = -(\partial E_\sigma / \partial d)$ and $F_{\text{mag}}(d) = -(\partial E_{\text{mag}} / \partial d)$ which are plotted in Fig. 6. A first interesting feature is that $F_\sigma(d)$ cancels out for $d \sim 20$ nm, which thus would be an equilibrium diameter for the skyrmion in the absence of the domain magnetostatic energy. This equilibrium is the result of a balance between the DW energy cost which is proportional to d and tends to decrease the skyrmion diameter and the curvature energy cost due to the exchange energy which scales as $1/d$ (ref. 34). However, the magnetostatic force F_{mag} is large enough at low diameter to destabilize this balance and the final equilibrium position is obtained for a larger value of $d \sim 90$ nm, where the two forces are equal. This underlines that the magnetostatic energy plays an important role in the stability and size of the skyrmion at zero external magnetic field. We also carried out micromagnetic simulations for square nanostructures with larger lateral dimensions. We observed that for sides larger than 1.2 μm , the skyrmion structure is not stable and a stripe domain structure appears. This may explain why we did not observe any skyrmions but stripe domains for larger structures with 1 μm sides (see Supplementary Information). Thus, the

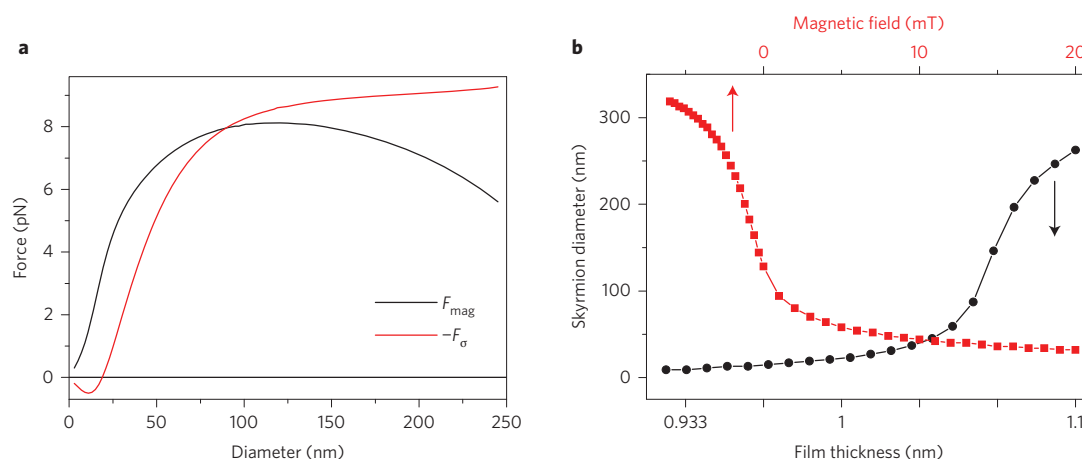


Figure 6 | Forces acting on the skyrmion and dependence of the skyrmion diameter on a perpendicular magnetic field and the film thickness.

a, Forces acting on the DW as a function of the skyrmion diameter. F_{σ} is the force due to the exchange and effective anisotropy, F_{mag} is the force due to the magnetostatic interaction between the domains. **b**, Skyrmion diameter as a function of the film thickness (black dots) and as a function of a perpendicular external magnetic field (red squares) for $t = 1.06$ nm computed using micromagnetic simulations.

confinement is an additional important feature for the skyrmion stability.

It may seem surprising that the domain magnetostatic energy plays such an important role in the skyrmion stability given the small thickness of the layer. Indeed, magnetostatic effects are expected to favour multidomain states only when the film thickness t is of the order or larger than the characteristic length $l_w = \sigma / (\mu_0 M_s^2)$, where σ is the DW surface energy. This criterion expresses the competition between the cost in the DW energy and the gain in the magnetostatic energy when creating a domain. The energy σ scales as $\sigma \sim 4\sqrt{AK_{\text{eff}}} - \pi D$ so that it is decreased in the presence of DMI. Thus, the criterion $l_w \sim t$ can be fulfilled even for very low thickness. In our experiments, we find that l_w is indeed of the order of the film thickness, $l_w \sim 1$ nm. This leads to the counterintuitive conclusion that the higher the DMI, the larger the role played by the magnetostatic interaction in the skyrmion stability. Note that this holds for $\sigma > 0$, that is $D < D_c$ where $D_c = 4\sqrt{AK_{\text{eff}}}/\pi$, which is the case in our sample where $D/D_c = 0.8$.

Our analysis underlines that the lateral size of the skyrmion results from a fine balance between the DW energy modulated by the DMI and the magnetostatic interaction in the patterned structure. As these quantities depend on the film thickness t , an important impact of t on the skyrmion diameter and stability is expected. This is confirmed by micromagnetic simulations that show that the skyrmion structure is stable only within a narrow window of film thickness, between 0.9 and 1.1 nm for our material parameters and sample geometry (see Fig. 6b, black curve (K and D are assumed to scale as $1/t$)⁴¹). Within this window, the skyrmion diameter strongly depends on the film thickness and ranges between 10 and 250 nm. A similar variation of the skyrmion diameter is also observed when applying a small perpendicular magnetic field (Fig. 6b, red curve). These simulations are in agreement with the skyrmion diameter we observe experimentally for thicker Co layer (1.08 nm) and in the presence of H_z as shown in Fig. 5. A magnetic memory based on the manipulation of skyrmions by an in-plane current would typically require skyrmion of tens of nanometres in diameter for having a significant technological impact. Our simulations show that this can be reached by playing on the film thickness, or using a bias magnetic field, which can be generated by the stray field of a neighbouring magnetic layer or by exchange bias⁶⁰.

To conclude, we have observed stable magnetic skyrmions at room temperature in ultrathin Pt/Co/MgO nanostructures in the

absence of applied external magnetic field. Using the high-resolution XMCD-PEEM magnetic microscopy technique, we were able to demonstrate the skyrmion left-handed chiral Néel structure, which can be explained by the large DMI measured in this material. Micromagnetic simulations are in agreement with our experimental results and we show that the equilibrium skyrmion structure is the result of a balance between the domain wall energy modulated by the DMI and the magnetostatic interaction in the patterned structure. This balance is very sensitive to the different magnetic parameters that are D , K , A and the total magnetic moment. The lateral confinement also plays an important role as it leads to a modulation of the magnetostatic energy. Hence, the size and stability of magnetic skyrmions can be finely tuned by playing with these different parameters. This will be key for the design of future devices based on the manipulation of magnetic skyrmions.

Methods

Methods and any associated references are available in the [online version of the paper](#).

Received 13 July 2015; accepted 1 December 2015;
published online 25 January 2016

References

- Bogdanov, A. N. & Yablonskii, D. Thermodynamically stable “vortices” in magnetically ordered crystals. the mixed state of magnets. *J. Exp. Theor. Phys.* **95**, 178 (1989).
- Rößler, U. K., Bogdanov, A. N. & Pflüderer, C. Spontaneous skyrmion ground states in magnetic metals. *Nature* **442**, 797–801 (2006).
- Mühlbauer, S. *et al.* Skyrmion lattice in a chiral magnet. *Science* **323**, 915–919 (2009).
- Pappas, C. *et al.* Chiral paramagnetic skyrmion-like phase in MnSi. *Phys. Rev. Lett.* **102**, 197202 (2009).
- Yu, X. Z. *et al.* Real-space observation of a two-dimensional skyrmion crystal. *Nature* **465**, 901–904 (2010).
- Nagaosa, N. & Tokura, Y. Topological properties and dynamics of magnetic skyrmions. *Nature Nanotech.* **8**, 899–911 (2013).
- Fert, A., Cros, V. & Sampaio, J. Skyrmions on the track. *Nature Nanotech.* **8**, 152–156 (2013).
- Braun, H.-B. Topological effects in nanomagnetism: from superparamagnetism to chiral quantum solitons. *Adv. Phys.* **61**, 1–116 (2012).
- Moriya, T. Anisotropic superexchange interaction and weak Ferromagnetism. *Phys. Rev.* **120**, 91–98 (1960).
- Dzyaloshinskii, I. E. *Sov. Phys. JETP* **5**, 1259 (1957).
- Jonietz, F. *et al.* Spin transfer torques in MnSi at ultralow current densities. *Science* **330**, 1648–1651 (2010).

12. Schulz, T. *et al.* Emergent electrodynamics of skyrmions in a chiral magnet. *Nat Phys* **8**, 301–304 (2012).
13. Yu, X. Z. *et al.* Skyrmion flow near room temperature in an ultralow current density. *Nature Commun.* **3**, 988 (2012).
14. Jiang, W. *et al.* Blowing magnetic skyrmion bubbles. *Science* **349**, 283 (2015).
15. Koshibae, W. *et al.* Memory functions of magnetic skyrmions. *Japan. J. Appl. Phys.* **54**, 053001 (2015).
16. Zhang, X., Ezawa, M. & Zhou, Y. Magnetic skyrmion logic gates: conversion, duplication and merging of skyrmions. *Sci. Rep.* **5**, 9400 (2015).
17. Moutafis, C., Komineas, S. & Bland, J. A. C. Dynamics and switching processes for magnetic bubbles in nanoelements. *Phys. Rev. B* **79**, 224429 (2009).
18. Büttner, F. *et al.* Dynamics and inertia of skyrmionic spin structures. *Nature Phys.* **11**, 225–228 (2015).
19. Sampaio, J., Cros, V., Rohart, S., Thiaville, A. & Fert, A. Nucleation, stability and current-induced motion of isolated magnetic skyrmions in nanostructures. *Nature Nanotech.* **8**, 839–844 (2013).
20. Tomasello, R. *et al.* A strategy for the design of skyrmion racetrack memories. *Sci. Rep.* **4**, 6784 (2014).
21. Iwasaki, J., Mochizuki, M. & Nagaosa, N. Current-induced skyrmion dynamics in constricted geometries. *Nature Nanotech.* **8**, 742–747 (2013).
22. Zhou, Y. & Ezawa, M. A reversible conversion between a skyrmion and a domain-wall pair in a junction geometry. *Nature Commun.* **5**, 4652 (2014).
23. Zhang, X. *et al.* Skyrmion-skyrmion and skyrmion-edge repulsions in skyrmion-based racetrack memory. *Sci. Rep.* **5**, 7643 (2015).
24. Yu, X. Z. *et al.* Real-space observation of a two-dimensional skyrmion crystal. *Nature* **465**, 901–904 (2010).
25. Yu, X. Z. *et al.* Near room-temperature formation of a skyrmion crystal in thin-films of the helimagnet FeGe. *Nature Mater.* **10**, 106–109 (2011).
26. Shibata, K. *et al.* Towards control of the size and helicity of skyrmions in helimagnetic alloys by spin-orbit coupling. *Nature Nanotech.* **8**, 723–728 (2013).
27. Heinze, S. *et al.* Spontaneous atomic-scale magnetic skyrmion lattice in two dimensions. *Nature Phys.* **7**, 713–718 (2011).
28. Romming, N. *et al.* Writing and deleting single magnetic skyrmions. *Science* **341**, 636–639 (2013).
29. Romming, N., Kubetzka, A., Hanneken, C., von Bergmann, K. & Wiesendanger, R. Field-dependent size and shape of single magnetic skyrmions. *Phys. Rev. Lett.* **114**, 177203 (2015).
30. Bogdanov, A. & Hubert, A. Thermodynamically stable magnetic vortex states in magnetic crystals. *J. Magn. Magn. Mater.* **138**, 255–269 (1994).
31. Bogdanov, A. & Hubert, A. The stability of vortex-like structures in uniaxial ferromagnets. *J. Magn. Magn. Mater.* **195**, 182–192 (1999).
32. Sonntag, A., Hermenau, J., Krause, S. & Wiesendanger, R. Thermal stability of an interface-stabilized skyrmion lattice. *Phys. Rev. Lett.* **113**, 077202 (2014).
33. Monso, S. *et al.* Crossover from in-plane to perpendicular anisotropy in Pt/CoFe/AlO_x sandwiches as a function of Al oxidation: A very accurate control of the oxidation of tunnel barriers. *Appl. Phys. Lett.* **80**, 4157–4159 (2002).
34. Rohart, S. & Thiaville, A. Skyrmion confinement in ultrathin film nanostructures in the presence of Dzyaloshinskii-Moriya interaction. *Phys. Rev. B* **88**, 184422 (2013).
35. Freimuth, F., Blügel, S. & Mokrousov, Y. Berry phase theory of Dzyaloshinskii-Moriya interaction and spin-orbit torques. *J. Phys. Condens. Matter* **26**, 104202 (2014).
36. Emori, S. *et al.* Spin hall torque magnetometry of Dzyaloshinskii domain walls. *Phys. Rev. B* **90**, 184427 (2014).
37. Pizzini, S. *et al.* Chirality-induced asymmetric magnetic nucleation in Pt/Co/AlO_x ultrathin microstructures. *Phys. Rev. Lett.* **113**, 047203 (2014).
38. Di, K. *et al.* Asymmetric spin-wave dispersion due to Dzyaloshinskii-Moriya interaction in an ultrathin Pt/CoFeB film. *Appl. Phys. Lett.* **106**, 052403 (2015).
39. Nembach, H. T., Shaw, J. M., Weiler, M., Jué, E. & Silva, T. J. Linear relation between Heisenberg exchange and interfacial Dzyaloshinskii-Moriya interaction in metal films. *Nature Phys.* **11**, 825–829 (2015).
40. Stashkevich, A. A. *et al.* Experimental study of spin-wave dispersion in Py/Pt film structures in the presence of an interface Dzyaloshinskii-Moriya interaction. *Phys. Rev. B* **91**, 214409 (2015).
41. Belmeguenai, M. *et al.* Interfacial Dzyaloshinskii-Moriya interaction in perpendicularly magnetized Pt/Co/AlO_x ultrathin films measured by Brillouin light spectroscopy. *Phys. Rev. B* **91**, 180405 (2015).
42. Yang, H., Thiaville, A., Rohart, S., Fert, A. & Chshiev, M. Anatomy of Dzyaloshinskii-Moriya interaction at Co/Pt interfaces. *Phys. Rev. Lett.* **115**, 267210 (2015).
43. Chen, G. *et al.* Novel chiral magnetic domain wall structure in Fe/ Ni/Cu(001) films. *Phys. Rev. Lett.* **110**, 177204 (2013).
44. Tetienne, J.-P. *et al.* The nature of domain walls in ultrathin ferromagnets revealed by scanning nanomagnetometry. *Nature Commun.* **6**, 6733 (2015).
45. Miron, I. M. *et al.* Perpendicular switching of a single ferromagnetic layer induced by in-plane current injection. *Nature* **476**, 189–193 (2011).
46. Garello, K. *et al.* Symmetry and magnitude of spin-orbit torques in ferromagnetic heterostructures. *Nature Nanotech.* **8**, 587–593 (2013).
47. Miron, I. M. *et al.* Fast current-induced domain-wall motion controlled by the Rashba effect. *Nature Mater.* **10**, 419–423 (2011).
48. Thiaville, A., Rohart, S., Jué, É., Cros, V. & Fert, A. Dynamics of Dzyaloshinskii domain walls in ultrathin magnetic films. *Europhys. Lett.* **100**, 57002 (2012).
49. Moreau-Luchaire, C. *et al.* Additive interfacial chiral interaction in multilayers for stabilization of small individual skyrmions at room temperature. *Nature Nanotech.* <http://dx.doi.org/10.1038/nnano.2015.313> (2016).
50. Woo, S. *et al.* Observation of room temperature magnetic skyrmions and their current-driven dynamics in ultrathin Co films. Preprint at <http://arxiv.org/abs/1502.07376> (2015).
51. Slonczewski, J. & Malozemoff, A. P. *Magnetic Domain Walls in Bubble Materials* (Academic, 1979).
52. Hehn, M. *et al.* Nanoscale magnetic domains in mesoscopic magnets. *Science* **272**, 1782–1785 (1996).
53. Moutafis, C. *et al.* Magnetic bubbles in FePt nanodots with perpendicular anisotropy. *Phys. Rev. B* **76**, 104426 (2007).
54. Braun, H.-B. Fluctuations and instabilities of ferromagnetic domain-wall pairs in an external magnetic field. *Phys. Rev. B* **50**, 16485–16500 (1994).
55. Kubetzka, A., Pietzsch, O., Bode, M. & Wiesendanger, R. Spin-polarized scanning tunneling microscopy study of 360° walls in an external magnetic field. *Phys. Rev. B* **67**, 020401 (2003).
56. Metaxas, P. J. *et al.* Creep and flow regimes of magnetic domain-wall motion in ultrathin Pt/Co/Pt films with perpendicular anisotropy. *Phys. Rev. Lett.* **99**, 217208 (2007).
57. Kiselev, N. S., Bogdanov, A. N., Schäfer, R. & Rössler, U. K. Chiral skyrmions in thin magnetic films: new objects for magnetic storage technologies? *J. Phys. D* **44**, 392001 (2011).
58. Braun, H.-B. Nucleation in ferromagnetic nanowires—magnetostatics and topology. *J. Appl. Phys.* **85**, 6172–6174 (1999).
59. Guslienko, K. Skyrmion state stability in magnetic nanodots with perpendicular anisotropy. *IEEE Magn. Lett.* **6**, 1–4 (2015).
60. Chen, G., Mascaraque, A., N'Diaye, A. T. & Schmid, A. K. Room temperature skyrmion ground state stabilized through interlayer exchange coupling. *Appl. Phys. Lett.* **106**, 242404 (2015).

Acknowledgements

The authors would like to thank A. Thiaville, M. Cubukcu, L. Camosi, M. Caminale and W. Saverio-Torres for discussions and their help in experiments. For their contribution to the CIRCE beamline at the Alba synchrotron, we would like to thank C. Escudero, V. Perez-Dieste, E. Pellegrin, J. Nicolas and S. Ferrer. S.P. and J.V. acknowledge the support of the Agence Nationale de la Recherche, project ANR-14-CE26-0012 (ULTRASKY).

Author contributions

O.B. conceived and designed the experiments. O.B., J.V., S.P., D.S.C., A.L., T.O.M., A.S., L.A., M.F. participated in the XMCD-PEEM experiments. O.B. and J.V. analysed the microscopy data. H.Y. and M.C. carried out the *ab initio* calculations. O.B., L.B.-D. and O.K. carried out the micromagnetic simulations, O.B. carried out the numerical calculations, S.A. deposited the magnetic multilayers, M.B., Y.R., A.S. carried out the BLS experiments. O.B. wrote the manuscript. All authors discussed the results and commented on the manuscript.

Additional information

Supplementary information is available in the [online version of the paper](#). Reprints and permissions information is available online at www.nature.com/reprints. Correspondence and requests for materials should be addressed to O.B.

Competing financial interests

The authors declare no competing financial interests.

Methods

Sample preparation and magnetic microscopy experiment. The Ta(3)/Pt(3)/Co (0.5–1)/MgO_x/Ta(1) (thickness in nm) film was deposited by magnetron sputtering on a 100 mm high-resistivity Si wafer, then annealed for 1.5 h at 250 °C under vacuum and an in-plane magnetic field of 240 mT. The Co layer was deposited as a wedge using a rotating cover during the deposition. The nominal thickness at the position of observation is $t = 0.98$ nm, except in the sample corresponding to Fig. 5, where $t = 1.08$ nm. The samples were patterned in different shapes (circle, square) and sizes using standard nanofabrication techniques. The XMCD-PEEM magnetic microscopy experiments were carried out with the SPELEEM III microscope (Elmitec GmbH) at the Nanospectroscopy beamline⁶¹ at the Elettra synchrotron in Basovizza, Trieste, Italy and at the CIRCE beamline with the collaboration of ALBA staff⁶². To fit the linescan of Fig. 1b, the standard deviation of the spatial Gaussian convolution σ is used as a free parameter leading to $2\sigma = 40$ nm (see Supplementary Information). In Fig. 3b, σ is deduced from a fit of a linescan of the topological image of the dot with an error function. This leads to $2\sigma = 28$ nm.

Brillouin light scattering experiments. The BLS experiments setup and conditions are the same as those described in ref. 41. A backscattering geometry has been used. The investigated spin wave vector lies in the plane of incidence and its length is $k_x = 4\pi \sin(\theta_{\text{inc}})/\lambda$ (where θ_{inc} is the angle of incidence and $\lambda = 532$ nm is the wavelength of the illuminating laser). The external magnetic field was applied perpendicularly to the incidence plane, which allows spin waves propagating along the in-plane direction perpendicular to the applied field to be probed (Damon–Eshbach geometry).

Micromagnetic simulations. The micromagnetic simulations were carried out using different micromagnetic codes: a homemade code⁶³, the Mumax3 code⁶⁴, and the OOMMF code⁶⁵. The following parameters were used (see Supplementary Information): $K = 1.45 \times 10^6$ J m⁻³, $M_s = 1.4 \times 10^6$ A m⁻¹, $A = 27.5$ pJ m⁻¹, $D = 2.05$ mJ m⁻² and a film thickness $t = 1.06$ nm. The lateral size of the elementary cells was typically between 1 and 3 nm. The results presented in this Article were obtained for a lateral cell size of 1 nm. In Fig. 6b, a spatial Gaussian convolution with

standard deviation $\sigma = 14$ nm was used to simulate the finite lateral spatial resolution of the microscope.

Numerical calculations of the skyrmion energy. $E_0(d)$ was calculated numerically by minimizing E_0 with respect to the domain wall width Δ at fixed d . $E_{\text{mag}}(d)$ was then evaluated from the total magnetostatic energy $E_{\text{mag}0}$ of a Bloch DW in a 420-nm-diameter circular dot using ref. 59.

$$E_{\text{mag}}(d) = E_{\text{mag}0} - t(1 - N_{\text{DW}}) \frac{\mu_0 M_s^2}{2} \int_0^R \cos^2 \theta \, 2\pi r dr \text{ with}$$

$$E_{\text{mag}0} = \frac{4\pi t}{R} \int_0^\infty [1 - \exp(-\beta x)] I^2(x) dx$$

$$I(x) = \int_0^1 dr' r' J_0(xr') \cos \theta(r')$$

where $r' = r/R$ and J_0 is the Bessel function of order zero. R is the dot radius. $N_{\text{DW}} = 0.0188$ was deduced from the width of the DW predicted by the micromagnetic simulations.

References

- Menteş, T. O., Zamborlini, G., Sala, A. & Locatelli, A. *Beilstein J. Nanotechnol.* **5**, 1873886 (2014).
- Aballe, L., Foerster, M., Pellegrin, E., Nicolas, J. & Ferrer, S. The ALBA spectroscopic LEEM-PEEM experimental station: layout and performance. *J. Synchrotron Radiat.* **22**, 745–752 (2015).
- Buda, L. D., Prejbeanu, I. L., Ebels, U. & Ounadjela, K. Micromagnetic simulations of magnetisation in circular cobalt dots. *Comput. Mater. Sci.* **24**, 181 (2002).
- Vansteenkiste, A. & Van de Wiele, B. MuMax: A new high-performance micromagnetic simulation tool. *J. Magn. Magn. Mater.* **323**, 2585–2591 (2011).
- Donahue, M. J. & Porter, D. G. *OOMMF User's Guide* version 1.0 (National Institute of Standards and Technology, 1999).